*remote sensing*

MDPI

*Article*

# Sentinel-2A MSI and Landsat 8 OLI Provide Data Continuity for Geological Remote Sensing

**Harald van der Werff * and Freek van der Meer**

Faculty of Geo-information Science and Earth Observation, University of Twente, Drienerlolaan 5, 7522 NB Enschede, The Netherlands

* Correspondence: harald.vanderwerff@utwente.nl

Academic Editors: Clement Atzberger and Prasad S. Thenkabail

Received: 31 August 2016 / Accepted: 12 October 2016 / Published: 25 October 2016

**Abstract:** Sentinel-2A MSI is the Landsat-like spatial resolution (10–60 m) super-spectral instrument of the European Space Agency (ESA), aimed at additional data continuity for global land surface monitoring with Landsat and Satellite Pour l'Observation de la Terre (SPOT) missions. Several simulation studies have been conducted in the last several years to show the potential of Sentinel-2A MSI (MultiSpectral Instrument). Now that real data are available, the first confirmations of this potential and comparisons with other operational systems are being made. This paper aims at evaluating Sentinel-2A MSI band ratio products that are relevant for geological remote sensing. A Sentinel-2A MSI and a Landsat 8 OLI (Operational Land Imager) scene were processed from their respective levels L1C and L1T to level L2A (bottom of atmosphere reflectance). Then, three band ratios originally defined for Landsat TM (Thematic Mapper) were used to map mineralogy associated with a hydrothermal alteration system in southeast Spain. The results obtained with Sentinel-2A MSI were compared with those obtained with Landsat 8 OLI and a simulated Sentinel-2A MSI dataset that was used before actual data were released. Results show that the images appear similar to the human eye having a correlation of approximately 0.8 and higher, but that the associated data ranges differ significantly. The resulting products are also compared to a published geologic map of the study area, and it is shown that the resulting maps correspond with the conceptual geologic model of the epithermal deposit.

**Keywords:** Sentinel-2A MSI; Landsat 8 OLI; geology; alteration; band ratios; simulation; Cabo de Gata; Rodalquilar

---

## 1. Introduction

The European Commission (EC) and European Space Agency (ESA) established the European Earth Observation programme Copernicus for monitoring of the environment. The space component of this programme consists of five missions: Sentinel 1–5 [1]. These missions are to provide routine observations for operational Copernicus services and data continuity for already operational satellite systems [2]. Sentinel-2 carries a super-spectral imager with 13 bands covering the Visible and Near InfraRed (VNIR) and ShortWave InfraRed (SWIR) wavelength region. The spatial resolution of these bands is 10–60 m and has a coverage between −56 and +84 degrees latitude with a 290 km swath width. The minimum revisit time at the equator is 10 days for Sentinel-2A, which will decrease to five days when both planned imagers are operational [2]. When combined, the Sentinel-2A MSI (MultiSpectral Instrument) and Landsat 8 OLI (Operational Land Imager) sensors will provide a 10–30 m multi-spectral global coverage approximately every three days [3]. The Sentinel-2A satellite was launched on 23 June 2015 and the first scenes were delivered a few days later [4].

The potential of Sentinel-2A MSI encompasses a wide range of applications [5]. Based on simulated datasets, several data exploitation methods have been published in the preparation for this mission, with the majority comprising vegetation related studies: Leaf Area Index (LAI) [6–8]; chlorophyll and nitrogen [9]; biophysical parameters [10,11]; red edge position [9,12]; and vegetation state [13]. Outside the green realm are evaluation of water quality [14] and mapping of coral reefs [15]. The use of Sentinel-2A MSI for geological remote sensing was first evaluated by Van der Meer et al. [16], who compared the capabilities of Sentinel-2A MSI to the ASTER (Advanced Spaceborne Thermal Emission and Reflectance Radiometer) imager onboard the Terra satellite for mapping surface mineralogy associated with hydrothermal alteration systems.

In the 1980s, the Landsat MultiSpectral Scanner (MSS) was deployed for the first time to derive iron oxide maps [17]. With the advent of the Landsat Thematic Mapper (TM), band ratios were used to separate argillic from non-argillic materials (using TM bands 5/7) and for mapping ferric/ferrous oxides (using TM bands 3/1). Since the year 2000, the ASTER sensor [18–20] has been the work horse of geologic remote sensing for mapping surface mineralogy. Cudahy and Hewson [21] published several ASTER band ratios that serve as proxies for mineralogy; some of these bands overlap with the bands of Sentinel-2A MSI (Figure 1). Van der Meer et al. [16] then also concluded that Sentinel-2A MSI bands can be used in band ratios that were originally defined with Landsat 5 TM or ASTER and are expected to provide data continuity for geological remote sensing. Mielke et al. [22] evaluated several current and next-generation satellite sensors, including Sentinel-2A MSI, for mapping the iron absorption feature depth in a band-ratio approach. They concluded that sensors like Sentinel-2A MSI are suitable for detection of Gossan with their method, and that they potentially can save costs when used for target detection prior to hyperspectral data acquisition. Van der Werff and van der Meer [23] demonstrated the capabilities of Sentinel-2A MSI for geological remote sensing by mapping iron oxide mineralogy. This was done by introducing a modelling approach on the 0.9 μm iron absorption feature using Sentinel-2A MSI's near-infrared (NIR) bands 6–9. This was, however, all done prior to the availability of real Sentinel-2A MSI data.

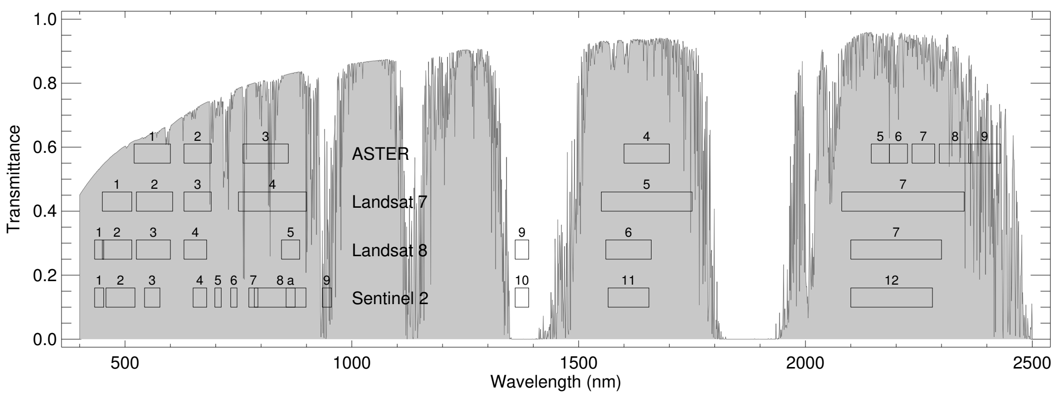


**Figure 1.** The width, wavelength positions and numbers of the Sentinel-2A MSI (MultiSpectral Instrument) spectral bands, in comparison to Landsat 8 OLI (Operational Land Imager), Landsat 5 TM (Thematic Mapper) and ASTER (Advanced Spaceborne Thermal Emission and Reflectance Radiometer). Atmospheric transmittance is plotted on the *y*-axis.

Now that actual Sentinel-2A MSI data are available, several studies have been undertaken to confirm prior findings. The majority comprises vegetation related studies, such as crop and tree species classification [24]; forest crowns [25,26]; chlorophyll and nitrogen [27] and biomass [28], as well as applications involving water, such as mapping water bodies [29]; water quality [30] and lake shore habitats [31].

This study aims to confirm the usability of Sentinel-2A MSI for geological remote sensing, as was laid out by Van der Meer et al. [16]. In their paper, a Sentinel-2A MSI dataset was simulated from a 2004 airborne hyperspectral image that covered a hydrothermal alteration area [32] near the former mining town of Rodalquilar, in the Sierra del Cabo de Gata in southeast Spain (Figure 2).

They compared their simulated Sentinel-2A MSI dataset to an ASTER scene for mapping alteration mineralogy using band ratios published for ASTER [33] and Landsat 5 TM [34]. In May 2016, a Sentinel-2A MSI and a Landsat 8 OLI image were acquired over the same area, in comparable weather conditions and season as when the hyperspectral dataset was acquired in 2004. This study aims to compare results of the Sentinel-2A MSI and Landsat 8 OLI imagery when applied for mapping alteration mineralogy, using band ratios developed for Landsat 5 TM [34]. As the geology and environmental conditions of the area have not really changed in the last 12 years, the results of 2016 are also compared with the simulated dataset dating from the year 2004, as used by Van der Meer et al. [16].

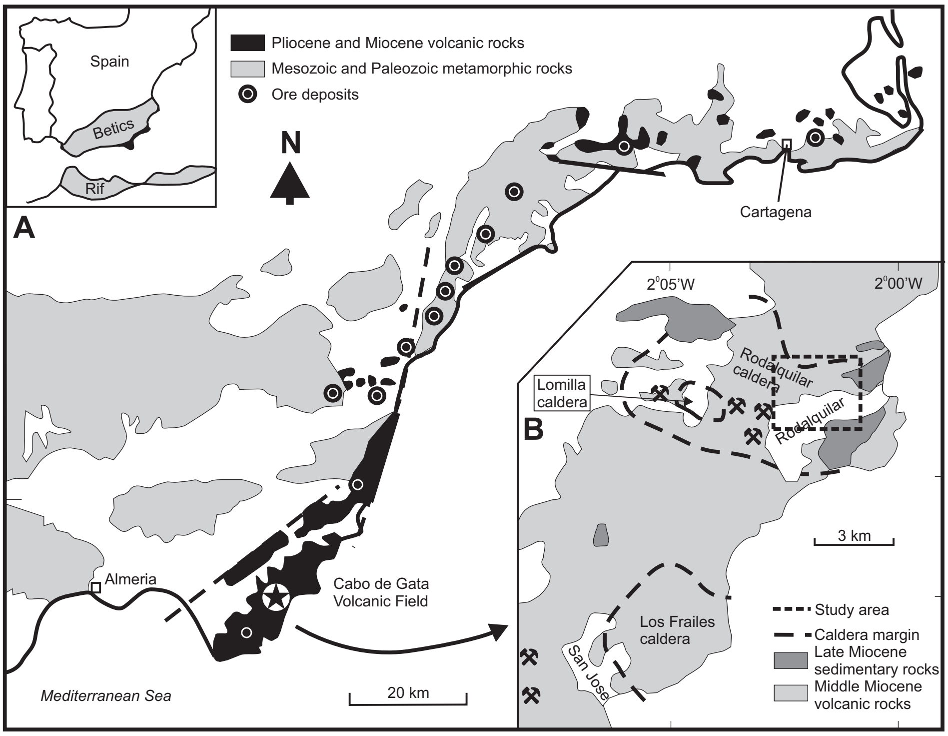


**Figure 2.** Location of the former mining town of Rodalquilar in the volcanic belt of southeast Spain (inset (**A**)) and the location of the image dataset used in this study (inset (**B**)). The Cabo de Gata volcanic field consists of calc-alkaline volcanic rocks (andesites and rhyolites) of late Tertiary age which have been extensively altered to form an assemblage of metamorphic minerals from high to low temperature as: silica, alunite, kaolinite, montmorillonite and chlorite. The geology, geochemistry and mineralization of the area is documented [35], while several remote sensing studies have been conducted at this site [36–39]. Image modified after Arribas et al. [35] and Rytuba et al. [32] and used with permission from Van der Meer et al. [16].

## 2. Method

The datasets analysed in this study are a Sentinel-2A MSI L1C image, a Landsat 8 OLI L1T image and a simulated Sentinel-2A MSI dataset. The latter is based on a geometrically corrected hyperspectral dataset that was previously processed to surface reflectance.

The Sentinel-2A MSI L1C dataset (12-bit radiometric quantization, 290 km swath width, ID S2A-OPER-MTD-SAFL1C-PDMC-20160526T103932-R051-V20160521T105553-20160521T105553, 21 May 2016 at 10:50 UTC, solar azimuth 127°, solar elevation 66°) was first atmospherically corrected with sen2cor software version 2.2.1 (Telespazio VEGA Deutschland GmbH, Darmstadt, Germany) [40] to level 2A, which is hemispherical-directional reflectance (HDRF) [41]. A pixel size of 20 m for the resulting level 2A product was chosen, as several band ratios require the 20 m resolution bands of Sentinel-2A MSI (see below). The resulting bottom-of-atmosphere reflectance dataset contained bands 1–7; 8a, 9, 11 and 12. The wide Near-Infrared (NIR) band 8, modelled after Landsat 5 TM and Satellite Pour l'Observation de la Terre (SPOT) 5, and band 10 used for detection of thin cirrus [2,42] were left out, leaving NIR band 8a to compare with Landsat 8 OLI. The data were spatially subset in SNAP version 2.0.2 (European Space Agency) [43] to the study area (originally 20,490 × 15,489 pixels; leaving 404 × 203 pixels starting at the top–left position $x = 9030$ and $y = 5931$). The resulting image is shown in Figure 3.

The Landsat 8 OLI L1T dataset (12-bit radiometric quantization, 190 km swath width, ID: LC81990352016145LGN00, 24 May 2016 at 10:44 UTC, solar azimuth 125°, solar elevation 66°) was radiometrically processed in IDL ENVI version 5.3 (Harris Corporation, Melbourne, FL, USA) [44] by applying the supplied gain and offset values. The L2 dataset was processed on demand by the U.S. Geological Survey Science Research and Development to surface reflectance, also being the hemispherical-directional reflectance factor (HDRF). The dataset was then subset to the study area delimited with Sentinel-2A MSI (leaving 269 × 135 pixels).

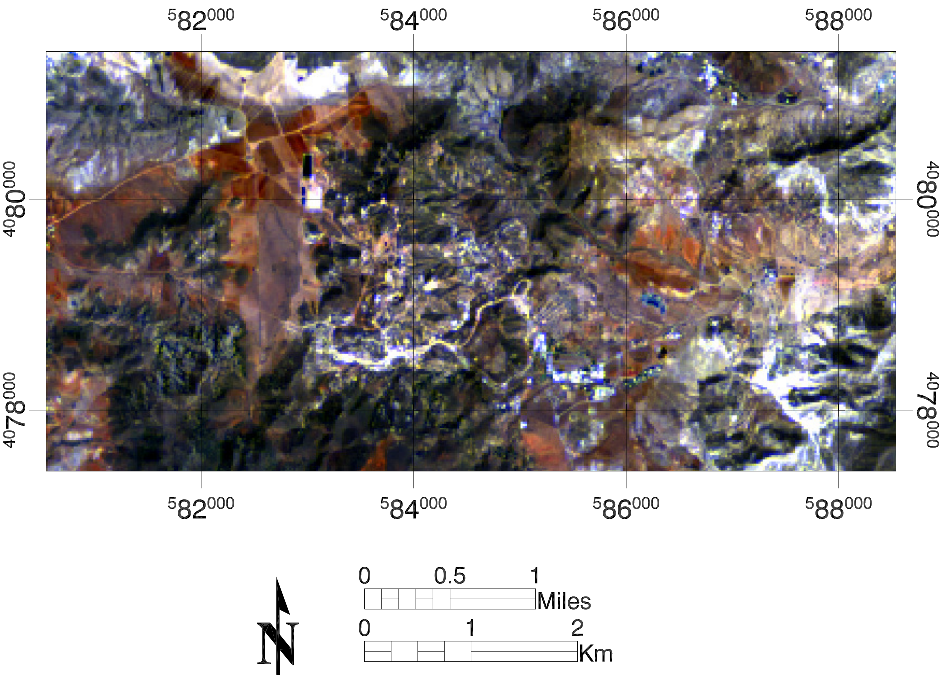


**Figure 3.** True colour composite of Sentinel-2A MSI bands 4 (in red), 3 (in green) and 2 (in blue). The image covers the 404 × 203 pixels subset of the study area around the mining town of Rodalquilar, Cabo de Gata, Spain.

The simulated Sentinel-2A MSI dataset used by Van der Meer et al. [16] is derived from a mosaic of HyMAP airborne hyperspectral images. The spectral coverage of HyMAP is nearly continuous in the VNIR and SWIR wavelength regions with small gaps in the middle of the 1.4 and 1.9 µm atmospheric water bands. The wavelength coverage, band width and spectral sampling interval for the 4 detectors are as follows: VIS 0.45–0.89 µm, 15–16 nm, 15 nm; NIR 0.89–1.35 µm, 15–16 nm, 15 nm; SWIR1 1.40–1.80 µm, 15–16 nm, 13 nm; SWIR2 1.95–2.48 µm, 18–20 nm, 17 nm. The spatial configuration of the instrument gives an Instantaneous Field Of View (IFOV) of 2.5 mrad along track and 2.0 mrad across track. The resulting scene that was used as a source for the simulated Sentinel-2A MSI dataset had originally a nominal pixel size of 4 × 4 m.

The HyMAP data (16 bit radiometric quantization) were acquired on 18 May 2004 by the German Aerospace Center (DLR) and processed to reflectance-at-surface values at a 4 m spatial sampling interval. This included geometric correction with PARGE (ReSe Applications Schläpfer, Zürich, Switzerland) [45] and a 5 m interval Digital Elevation Model (DEM), followed by an atmospheric correction with the ATCOR 4 (Atmospheric CORrection) software (ReSe Applications Schläpfer, Zürich, Switzerland) [46]. The HyMAP data were then spectrally convolved to the lower resolutions of the Sentinel-2A MSI bands using spectral response functions provided by ESA (see also [47]). After the spectral resampling, the data were spatially resampled from the original 4 m pixel resolution to the 20 m resolution of Sentinel-2A MSI bands. This was done following Kruse and Perry [48] using pixel aggregation (neighbourhood averaging). The subset of the study area was eventually covered by $402 \times 201$ pixels of $20 \times 20$ m.

For a statistical comparison, all three datasets were once more resampled to a 10 m grid covering $800 \times 400$ pixels. The geometric correction that comes with the images is not sufficiently accurate to allow a direct comparison. Visual inspection showed an offset of multiple pixels. The geometric correction was, however, found to be sufficiently precise, as hardly any internal deformation was observed. For this reason, it was decided not to follow an image-to-image matching approach as, for example, published by Yan et al. [3]. Instead, the low accuracy was manually corrected by shifting the Landsat 8 OLI image three pixels north ($y$-direction). The simulated dataset, based on a parametric geocoding, was shifted four pixels east ($x$-direction) and four pixels south ($y$-direction) in order to overlay the Sentinel-2A MSI image. The resulting datasets were subset to only include the pixels encompassed in all three datasets, leaving $790 \times 390$ pixels for comparative analysis. The weather conditions in the days before each data acquisition are in Table 1.

**Table 1.** Weather conditions in Almeria, Spain, in the week before the data acquisitions in 2004 and 2016 (indicated in grey). Data source is available online [49].

| | Temperature (°C) | | | Humidity (%) | | | Pressure (hPa) | Vis. (km) | Wind (km/h) | | Precip. (mm) | Events |
|---|---|---|---|---|---|---|---|---|---|---|---|---|
| | **High** | **Avg.** | **Low** | **High** | **Avg.** | **Low** | **Avg.** | **Avg.** | **High** | **Avg.** | **Sum** | |
| **May 2004** | | | | | | | | | | | | |
| 11 | 18 | 16 | 13 | 82 | 67 | 49 | 1009 | 10 | 37 | 14 | 0.00 | |
| 12 | 17 | 14 | 13 | 82 | 73 | 55 | 1014 | 10 | 11 | 6 | 0.00 | |
| 13 | 18 | 16 | 13 | 88 | 78 | 72 | 1015 | 9 | 14 | 6 | 0.00 | |
| 14 | 22 | 17 | 13 | 88 | 72 | 46 | 1016 | 8 | 39 | 11 | 0.00 | |
| 15 | 23 | 19 | 15 | 67 | 43 | 29 | 1020 | 10 | 42 | 24 | 0.00 | Fog |
| 16 | 23 | 18 | 14 | 59 | 40 | 31 | 1018 | 10 | 40 | 23 | 0.00 | |
| 17 | 25 | 19 | 14 | 67 | 47 | 29 | 1018 | 10 | 32 | 14 | 0.00 | |
| 18 | 25 | 20 | 16 | 59 | 41 | 29 | 1021 | 10 | 47 | 19 | 0.00 | |
| **May 2016** | | | | | | | | | | | | |
| 14 | 21 | 18 | 15 | 82 | 60 | 29 | 1016 | 10 | 27 | 16 | 0.00 | |
| 15 | 20 | 17 | 13 | 94 | 80 | 63 | 1018 | 10 | 11 | 5 | 0.00 | |
| 16 | 22 | 18 | 13 | 94 | 74 | 41 | 1020 | 9 | 11 | 3 | 0.00 | |
| 17 | 28 | 21 | 15 | 63 | 37 | 12 | 1016 | 16 | 37 | 11 | 0.00 | |
| 18 | 26 | 22 | 18 | 88 | 53 | 21 | 1016 | 10 | 24 | 11 | 0.00 | |
| 19 | 23 | 19 | 16 | 94 | 81 | 64 | 1016 | 9 | 13 | 5 | 0.00 | Fog |
| 20 | 28 | 23 | 18 | 94 | 53 | 17 | 1019 | 17 | 26 | 11 | 0.00 | |
| 21 | 29 | 23 | 17 | 83 | 43 | 13 | 1017 | 15 | 29 | 13 | 0.00 | |
| 22 | 24 | 20 | 16 | 88 | 70 | 48 | 1015 | 10 | 26 | 6 | 0.00 | |
| 23 | 27 | 22 | 17 | 88 | 53 | 21 | 1020 | 19 | 35 | 16 | 0.00 | |
| 24 | 23 | 20 | 16 | 88 | 71 | 44 | 1014 | 10 | 19 | 10 | 0.00 | |

Band ratios serve as proxies for mineral assemblages or individual mineral groups. A summary of Landsat 5 TM and ASTER band ratios suitable for use with Sentinel-2A MSI and Landsat 8 OLI is provided in Table 2. We focused on the band ratios originally defined for Landsat 5 TM by Sabins [34], which require bands 2 (Blue), 4 (Red), 6 (SWIR1) and 7 (SWIR2) of Landsat 8 OLI and bands 2, 4, 11 and 12 of Sentinel-2A MSI. In addition, Landsat 8 OLI band 5 (NIR) and Sentinel-2A MSI band 8a were needed for masking vegetation.

**Table 2.** Sentinel-2A MSI (MultiSpectral Instrument) and Landsat 8 OLI (Operational Land Imager) band ratios, as an analogue of Sabins [34] Landsat 5 TM (Thematic Mapper) and Kalinowski and Oliver [33] ASTER (Advanced Spaceborne Thermal Emission and Reflectance Radiometer) band ratios used as proxies for mapping mineralogy (modified after Van der Meer et al. [16]). The table is limited to band combinations that fall in the wavelength range of Sentinel-2A MSI.

| Feature | ASTER | Landsat 5 TM | Landsat 8 OLI | Sentinel-2A MSI |
|---|---|---|---|---|
| **TM Ratios** | | | | |
| Hydroxyl bearing alteration | 4/{5,6,7} | **5/7** | 6/7 | 11/12 |
| All iron oxides | – | **3/1** | 4/2 | 4/2 |
| Ferrous iron oxides | 2/4 | **3/5** | 4/6 | 4/11 |
| **ASTER Iron** | | | | |
| Ferric Iron, $Fe^{3+}$ | **2/1** | 3/2 | 4/3 | 4/3 |
| Ferrous Iron, $Fe^{2+}$ | **5/3 + 1/2** | 7/4 + 2/3 | 7/5 + 3/4 | 12/8 + 3/4 |
| Laterite | **4/5** | 5/7 | 6/7 | 11/12 † |
| Gossan | **4/2** | 5/3 | 6/4 | 11/4 |
| Ferrous silicates ‡ | **5/4** | 7/5 | 7/6 | 12/11 † |
| Ferric oxides | **4/3** | 5/4 | 6/5 | 11/8 |
| **ASTER Silicates** | | | | |
| Alteration | **4/5** | 5/7 | 6/7 | 11/12 † |
| **ASTER Other** | | | | |
| Vegetation | **3/2** | 4/3 | 5/4 | 8/4 |
| NDVI * | **(3 − 2)/(3 + 2)** | (4 − 3)/(4 + 3) | (5 − 4)/(5 + 4) | (8 − 4)/(8 + 4) |

† Band 12 of Sentinel-2A MSI and band 7 of Landsat 8 OLI cover ASTER bands 5–7. Landsat 5 TM band 7 also partially covers ASTER band 8; ‡ Biotite, chloride and amphibole; * Normalized Difference Vegetation Index.

First, the correlation between comparable bands of the Sentinel-2A MSI, Landsat 8 OLI and the simulated datasets were determined and interpreted with the help of scatterplots. Then, the Normalized Difference Vegetation Index (NDVI) was calculated for each dataset to prepare the masking of pixels with a vegetation cover. Although it was stated above that the environmental conditions of the area have not changed, it is likely that differences in vegetation cover do occur between 2004 and 2016. A vegetation index such as NDVI will, as a result, not be uniform for all scenes. It appeared that not only surface cover had changed over time, but also the range of values appeared to differ between the Sentinel-2A MSI and Landsat 8 OLI images acquired only three days apart. As no uniform thresholds could be defined, three vegetation masks were eventually created based on visual analysis, resulting in the following value ranges: 0–0.25 for Sentinel-2A MSI and Landsat 8 OLI and 0–0.4 for the simulated Sentinel-2A MSI dataset. The three resulting masks were subsequently fused and uniformly applied to all image datasets.

Three of the band ratios defined in Table 2 were selected for mapping the alteration mineralogy around the town of Rodalquilar: A combination that highlights hydroxyl bearing alteration (TM 5/7, Landsat 8 OLI 6/7 and Sentinel-2A MSI 11/12), a combination that highlights iron oxides in general (TM 3/1, Landsat 8 OLI 4/2 and Sentinel-2A MSI 4/2), and a combination that highlights ferrous iron oxides specifically (TM 3/5, Landsat 8 OLI 4/6 and Sentinel-2A MSI 4/11). The correlation between these products were also analysed in scatterplots, which are shown in Section 3. Lastly, the mineral alteration map obtained with Sentinel-2A MSI is compared with a published geological map [50].

## 3. Results

The comparison of the three datasets is shown as images and as scatterplots. In the scatterplots, the sensors are indicated with *S2A* (Sentinel-2A MSI), *LS8* (Landsat 8 OLI) and *Sim* (simulated Sentinel-2A MSI). Sentinel-2A MSI and Landsat 8 OLI results show both atmospherically corrected (L2A) datasets (indicated as bottom-of-atmosphere reflectance (BoA)) as well as the original data values of the L1T and L1C datasets (indicated as top-of-atmosphere reflectance (ToA)). The results of the simulated Sentinel-2A MSI dataset are only available in surface reflectance values.

Figure 4 shows the NDVI image results. Visually, a comparable spatial pattern can be seen in the Sentinel-2A MSI and Landsat 8 OLI results dating from May 2016. The simulated dataset, dating from May 2004, shows overall a similar pattern, but also shows a couple of differences that appear to be predominantly associated with agricultural fields (particularly in the northeast) and a mountain ridge (in the northwest). Although the patterns look similar in a 2%–98% image stretch, the range of NDVI values does differ considerably. The simulated dataset has the narrowest range (0.26–0.49), while Landsat 8 OLI has the widest range (0.06–0.61). The same is reflected in the scatterplots resulting from the NDVI products, which are shown in Figure 5. The correlation between Sentinel-2A MSI and Landsat 8 OLI is 0.85 for the bottom-of-atmosphere datasets (centre figure, S2a-BoA and LS8-BoA) and 0.82 for the top-of-atmosphere datasets (right figure, S2a-ToA and LS8-ToA). There is significantly more scatter between the bottom-of-atmosphere Sentinel-2A MSI dataset and the simulated Sentinel-2A MSI dataset (left figure, S2A-BoA and Sim). The high NDVI values that are associated with agricultural fields in the northeast of this scene even create a second population in the feature space, and makes the correlation drop to 0.40.

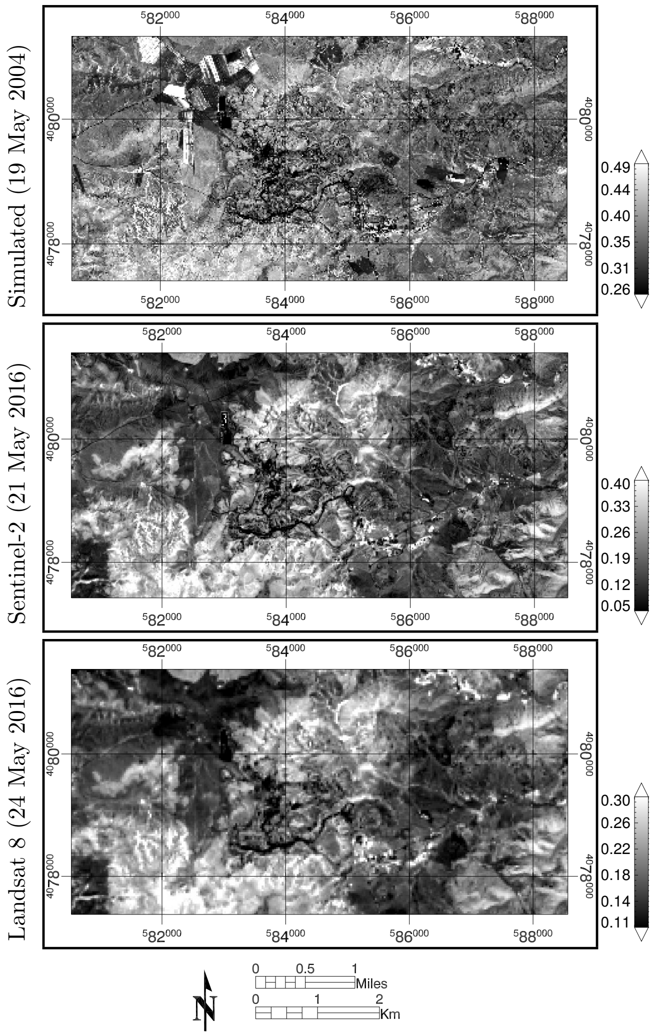


**Figure 4.** Normalized Difference Vegetation Index (NDVI) image result of the simulated Sentinel-2A MSI data cube dating from 2004 (**top**), the Sentinel-2A MSI dating from 2016 (**centre**), and the Landsat 8 OLI (**bottom**). The images shown are histogram stretched from 2%–98%. The town of Rodalquilar in the centre has relatively low NDVI values, while the hills north and south of it have the highest values. Other high values, such as those associated with the fields in the northeastern part of the simulated image, seem to be related to agricultural activity and not to geology.

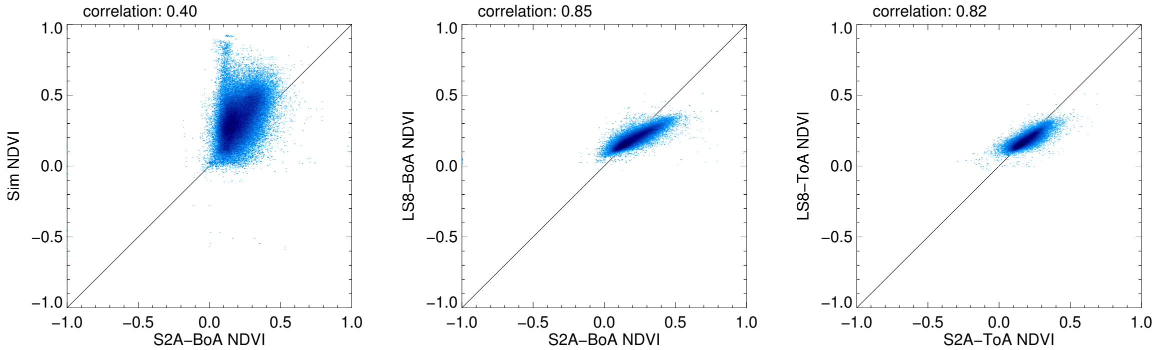


**Figure 5.** Scatterplots of the Normalized Difference Vegetation Index (NDVI) made with Landsat 8 OLI, Sentinel-2A MSI and a simulated Sentinel-2A MSI data cube. The figure on the **left** shows the scatter between the 2016 Sentinel-2A MSI bottom-of atmosphere (S2A-BoA) NDVI product and the 2004 simulated dataset (Sim). Note the relatively high values in the simulated datasets that are associated with the agricultural fields in the northeast of the scene. The **centre** figure shows the scatter between the 2016 Sentinel-2A MSI and Landsat 8 OLI bottom-of-atmosphere (S2A-BoA and LS8-BoA) products. The figure on the **right** shows the scatter between the Sentinel-2A MSI and Landsat 8 OLI top-of-atmosphere (S2A-ToA and LS8-ToA) products.

Figure 6 shows the image processing results for mapping mineral alteration with three band ratios for mapping mineralogy. When shown as colour composites, the three datasets are easily comparable to the human eye. Especially the ratio TM 5/7 (SWIR1/SWIR2, shown in red) shows similar patterns in all images. While the range of the Landsat 8 OLI ratio values is significantly higher (1.33–1.81) than both of the others, the data range for the two products based on the Sentinel-2A MSI band definitions (1.12–1.65 and 1.12–1.65) overlaps to a large extent. As a contrast, the spatial pattern for the ratio TM 3/1 (Red/Blue, shown in green) seems similar to the human eye for Landsat 8 OLI and Sentinel-2A MSI, but its presence in the simulated dataset is weaker. Between all three datasets, the data ranges also seem further apart. The ratio TM 3/5 (Red/SWIR1, shown in blue) shows similar data ranges for the two products based on Sentinel-2A MSI bands (0.40–0.72 and 0.40–0.72) and a significantly lower range for the Landsat 8 OLI product (0.27–0.43).

This result can be explained when looking at the scatterplots of these datasets in Figure 7. The correlation between the values of the Landsat 8 OLI and Sentinel-2A MSI bottom-of-atmosphere products is 0.95 for the TM 5/7 ratio (top row), 0.56 for the TM 3/1 ratio (centre) and 0.87 for the TM 3/5 ratio (bottom row). The correlation of the top-of-atmosphere reflectance products is higher than the bottom-of-atmosphere reflectance products (0.87 and 0.84 versus 0.56 and 0.78). The correlation between the Sentinel-2A MSI results of 2016 and the simulated dataset of 2004 (in the left column) is overall significantly lower, with correlations between 0.48 and 0.62. While the correlation is lower, it can however be observed that data ranges for band ratios 5/7 and 3/5 are similar, while between the Sentinel-2A MSI and Landsat 8 OLI bottom-of-atmosphere products, major differences appear in gain and offset. The Sentinel-2A MSI and Landsat 8 OLI top-of-atmosphere products suffer considerably less from this. Lastly, it can be observed that the two scatterplots that involve band 1 (blue) of the atmospherically corrected Sentinel-2A MSI products (center-left and centre-centre) both show a nonlinear trend. A comparison between the top-of-atmosphere and bottom-of-atmosphere products (Supplemental Materials) shows a correlations between 0.85 and 0.95, which does not reveal any abnormal behaviour for this particular band.

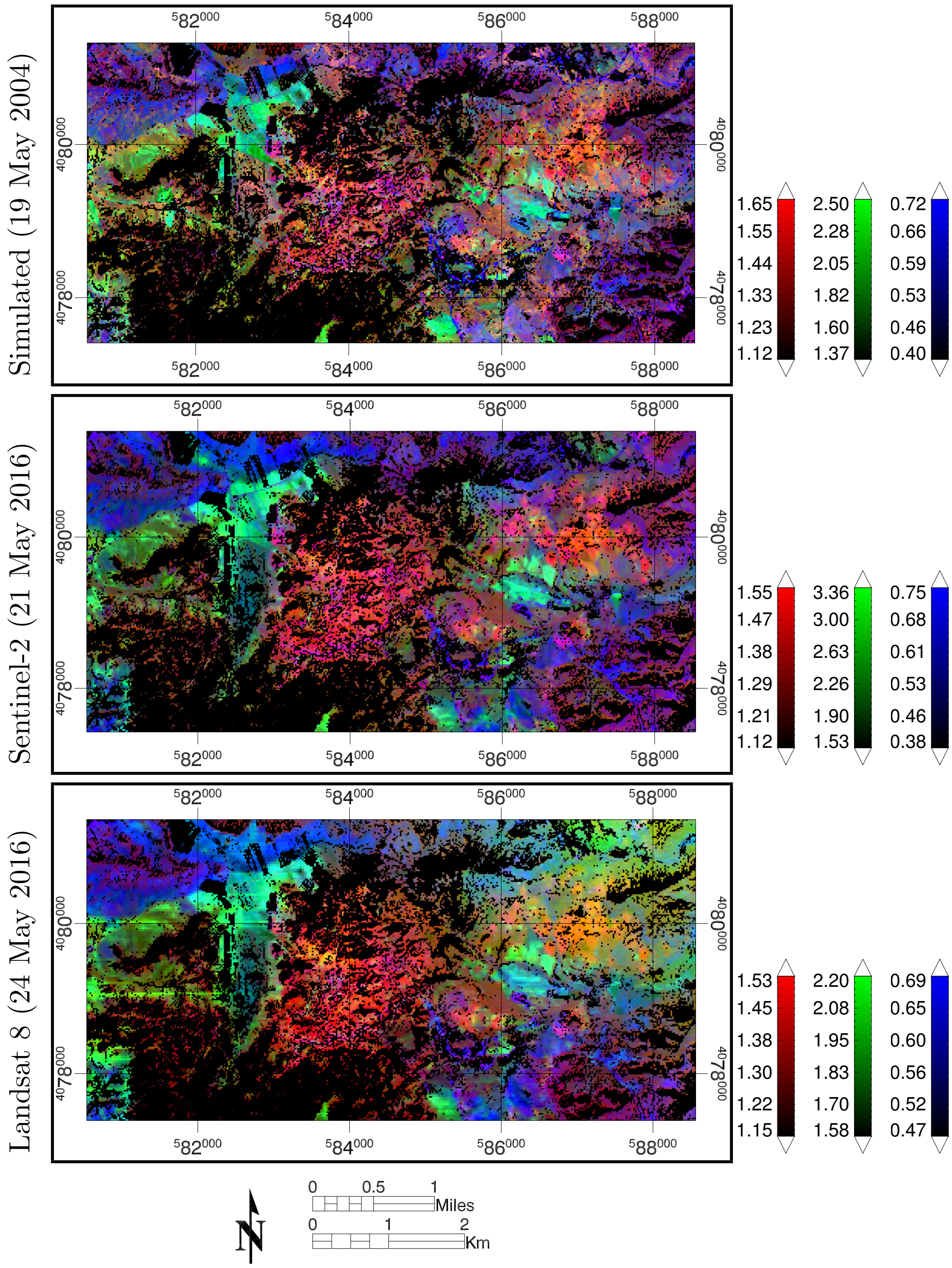


**Figure 6.** Sabins' band ratio colour composites of a simulated Sentinel-2A MSI data cube (**top**), Sentinel-2A MSI (**centre**) and Landsat 8 OLI (**bottom**). Shown are ratios TM 5/7 (ShortWave InfraRed 1/ShortWave InfraRed 2) in red, TM 3/1 (Red/Blue) in green and TM 3/5 (Red/ShortWave InfraRed 1) in blue. The patterns appear similar to the human eye, but differences can be observed in the ratio TM 3/1 between the simulated dataset of 2004 and the Landsat 8 OLI and Sentinel-2A MSI datasets of 2016. The colour ramps show that data ranges differ.

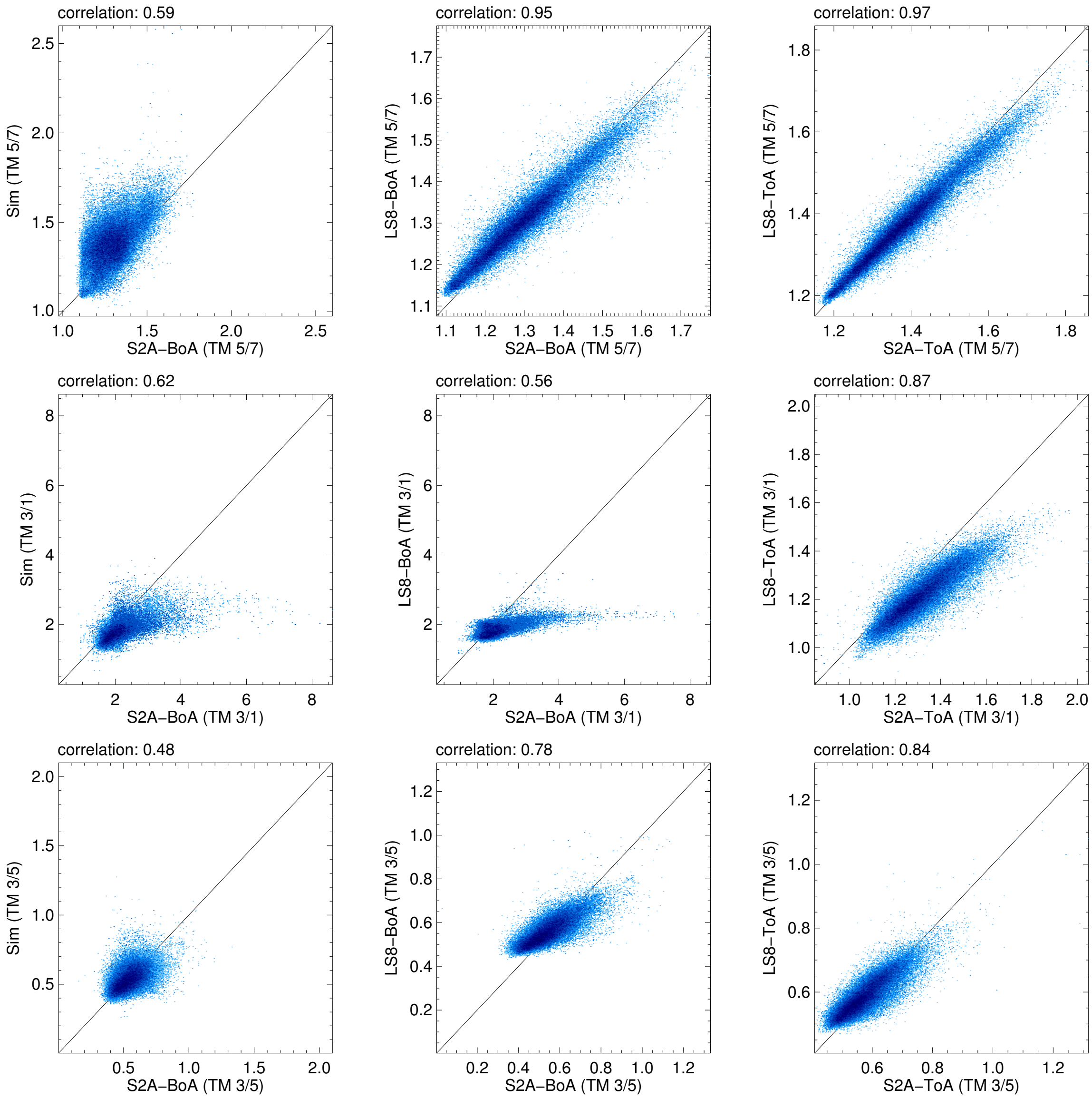


**Figure 7.** Scatterplots of Sabins' band ratios made with Landsat 8 OLI, Sentinel-2A MSI and a simulated Sentinel-2A MSI data cube. The **top** row shows ratio TM 5/7, the **centre** row shows ratio TM 3/1 and the **bottom** row shows ratio TM 3/5. It can be observed that the correlation between the top-of-atmosphere reflectance products is higher than the correlation between the bottom-of-atmosphere reflectance products.

Comparing the Sentinel-2A MSI band ratio product with the geological map, in Figure 8, shows that pixels with a relatively high value for TM 5/7 (hydroxyl bearing alteration, in red) coincide with Dacitic and Rhyolithic pyroclasts, domes and outflows (units 8, 10 and 11). It also appears that large parts of these volcanic rock units fall within image pixels that are masked, and are apparently covered by vegetation. The iron oxides, depicted in green and blue, are generally within the areas that have been mapped by Arribas [50] as quaternary deposits (unit 21).

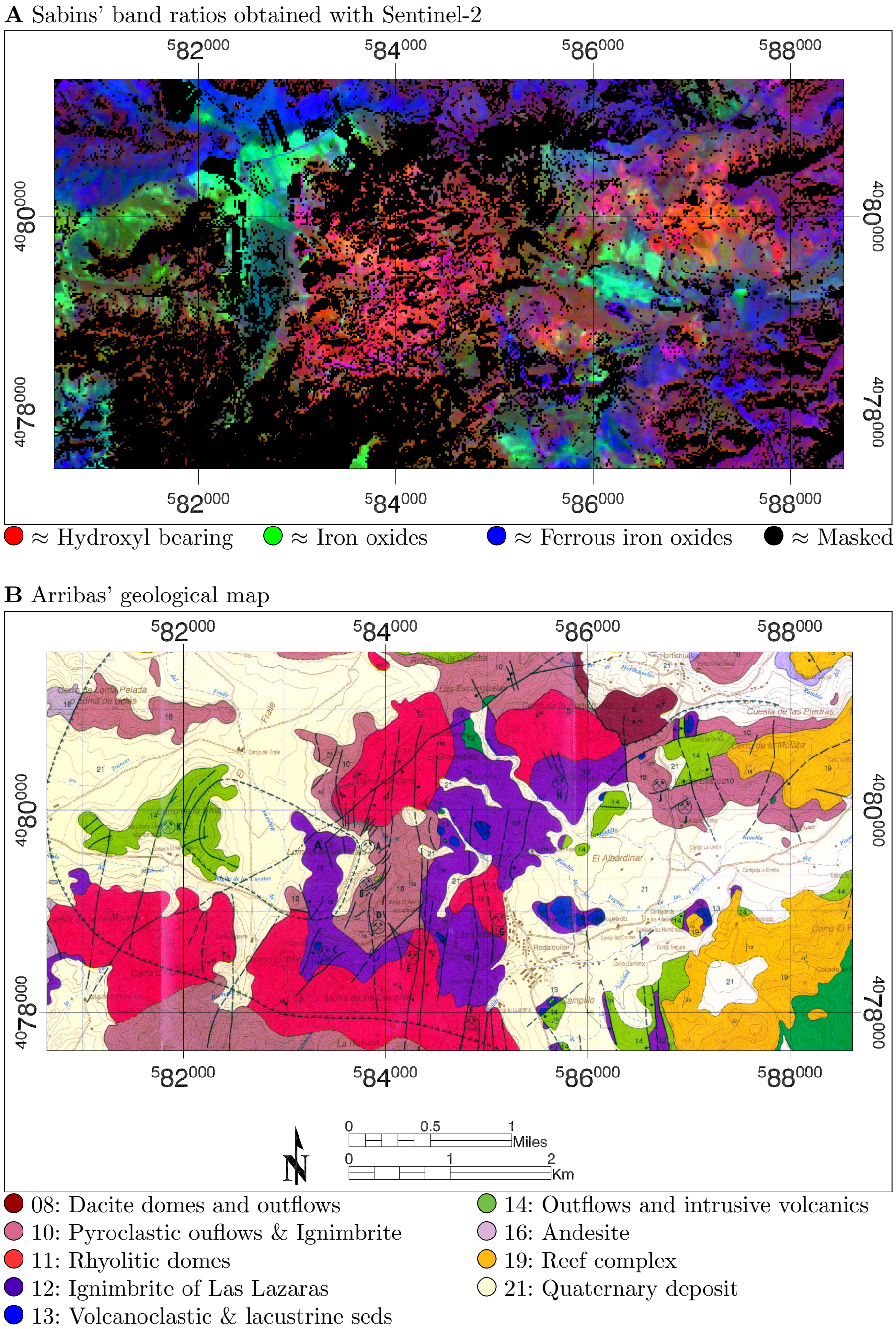


**Figure 8.** A colour composite made with Sentinel-2A MSI (**A**) consisting of band ratios TM 5/7 in red, 3/1 in green and 3/5 in blue. The patterns show a similarity with the volcanic rock units in the Rodalquilar area in a subset of a published geological map [50] (**B**).

## 4. Discussion

Three band ratios, previously defined for Landsat 5 TM, were used for mapping mineralogy associated with a hydrothermal alteration system in southeast Spain. The datasets were a subset of a Landsat 8 OLI and a Sentinel-2A MSI scene acquired in 2016 and a simulated Sentinel-2A MSI scene that was acquired in 2004. These data cover a geologically varied terrain, with marine limestones in the western part of the image, hills and slopes formed by highly altered volcanic tuffs containing sulfates and iron oxides in the centre part, and alluvial planes that contain eroded products from the surrounding hills. The surface cover of this area is complex. However, the similarity between the image products is, to the human eye, striking. Even when considering that the 12 years between the acquisition dates are not that relevant on a geological time scale, it must be concluded that, besides the vegetation cover in the agricultural fields, not much has changed in this area when it is observed with band ratios for depicting alteration mineralogy.

The similarity between the two multispectral scenes acquired in May 2016 is higher than the similarity with the dataset created from a hyperspectral scene acquired in May 2004. An explanation for this difference points towards land cover, weather and sensor differences. A small change in land cover might not easily be observed within single 10–20 m pixels. While the weather conditions of data acquisition both consisted of dry and sunny weather for several days in a row before data acquisition (Table 1), there may still remain a difference in how far the season (spring) was in either year.

The pre-processing done on the hyperspectral dataset involved a MODTRAN (MODerate resolution atmospheric TRANsmission) model to come to surface reflectance values. The correction applied to the Landsat 8 OLI dataset is based on the S6 atmospheric model, while the correction applied to the Sentinel-2A MSI dataset with the sen2cor software is based on "look-up tables compiled using an atmospheric radiative transfer model based on libRadtran1" [51]. The results in Figure 7 reveal that the Sentinel-2A MSI bottom-of-atmosphere band 2 does not compare as well as the top-of-atmosphere product does. Nevertheless, a direct comparison between the bottom-of-atmosphere and top-of-atmosphere product (Supplemental Materials) does not reveal a problem in the atmospheric correction.

Toming et al. [30], in their work on mapping lake water quality parameters with Sentinel-2A MSI, concluded that the currently provided atmospheric correction is in a need of improvement. However, most other studies [24–29,31] on initial results with Sentinel-2A MSI did not specifically mention this as an observation or a problem.

Overall, the obtained data products look similar and are likely to lead, when visually interpreted by one and the same end-user, to similar outcomes. This might well change when the products are interpreted or compared based on the values of the data products. Although the correlation between Landsat 8 OLI and Sentinel-2A MSI for this area and datasets was found to be in the range of 0.56–0.97, there are significant differences in the data ranges. In a (semi-)automated processing chain, an additional effort will be needed to make these data products repeatable in time and transportable between sensors. In our study, this became already apparent in the pre-processing of the data, when a masking of vegetation with NDVI had to be carried out manually due to the significant different data ranges that were obtained. This is, however, a common feature of remote sensing, and is not specific for the Sentinel-2A MSI or Landsat 8 OLI imagers in particular.

We have compared Sentinel-2A MSI with Landsat 8 OLI and used band ratios designed for Landsat family broadband multispectral sensors. ASTER band ratios have partially been ported to Sentinel-2A MSI by Van der Meer et al. [16], but these were not explored in detail in this study. However, this does not undermine the importance of Sentinel-2A MSI to also provide data continuity for ASTER. Despite the ASTER sensor going defunct in 2009 and the availability of a commercial high-spatial resolution sensor [52] that has four of ASTER's five SWIR bands, the use of ASTER for geological studies is still widespread. In any way, having a more frequent data acquisition is a welcome benefit.

The five to ten-day minimum revisit time of Sentinel-2A MSI is not only important for environmental studies that require frequent data: geological remote sensing would also benefit from frequent data. An example is the monitoring of geological activity associated with volcanoes, tectonics and geothermal systems, but also secondary effects related to earth sciences, such as land cover changes associated with natural degradation or natural hazards. However, the major leap that data continuity with operational satellite sensors such as Sentinel-2A MSI and Landsat 8 OLI can bring is the generation of physically consistent, reproducible and seamless data products, such as the seamless maps of surface mineralogy published for the continent Australia [53]. The future of geological remote sensing will incorporate the generation of such continental scale maps, and data continuity in time and space is therefore essential.

## 5. Conclusions

Three band ratios based on ESA's Sentinel-2A MSI were used to map mineralogy associated with a hydrothermal alteration system in southeastSpain. The results were compared with similar products derived from Landsat 8 OLI and a simulated Sentinel-2A MSI dataset used in Van der Meer et al. [16]. Although the surface cover of this area is complex in geological terms, a clear similarity between the image products can be observed with the human eye. When the products are, however, compared based on data values, it appears that particular band combinations have a considerable difference in gain and/or offset, despite also having an average correlation of approximately 0.8. Any specific problem with the atmospheric correction of Sentinel-2A MSI or Landsat 8 OLI could, however, not be found.

The resulting image products demonstrate a good correspondence between Sentinel-2A MSI and Landsat 8 OLI VNIR and SWIR bands. A number of band ratios originally proposed for Landsat 5 TM correlate favourably when ported to Sentinel-2A MSI. The resulting products are also compared to a published geologic map of the study area, and it is shown that the resulting maps support the existing conceptual geologic model of the epithermal deposit. The future of geological remote sensing will also incorporate the generation of continental scale maps that somehow have to be consistent in time and space. Sensor cross and inter-calibration as well as pre-processing methods, therefore, remain an important issue. Although the repeatability and portability of the Sentinel-2A MSI and Landsat 8 OLI data products is still a work in progress, this study shows that the Sentinel-2A MSI mission can provide data continuity for Landsat 8 OLI when studying mineralogy at the Earth surface.

**Supplementary Materials:** The following are available online at www.mdpi.com/2072-4292/8/11/883/s1, Figure S1: Scatterplots of Landsat 8 OLI bottom-of-atmosphere reflectance against top-of-atmosphere reflectance, Figure S2: Scatterplots of Landsat 8 OLI on-demand processed against QUick Atmospheric Correction (QUAC) bottom-of-atmosphere reflectance, Figure S3: Scatterplots of Sentinel-2A MSI bottom-of-atmosphere reflectance against top-of-atmosphere reflectance, Figure S4: Scatterplots of Sentinel-2A MSI sen2cor v.2.2.1 against sen2cor v.2.0.6 bottom-of-atmosphere reflectance, Figure S5: Scatterplots of Sentinel-2A MSI bottom-of-atmosphere reflectance against the Simulated data cube, Figure S6: Scatterplots of Sentinel-2A MSI bottom-of-atmosphere reflectance against Landsat 8 OLI bottom-of-atmosphere reflectance, Figure S7: Scatterplots of Sentinel-2A MSI top-of-atmosphere reflectance against Landsat 8 OLI top-of-atmosphere reflectance.

**Acknowledgments:** The authors are grateful to Michael Berger and Ferran Gascon Roca (ESA) for providing the Sentinel-2A MSI spectral response functions used in data simulation. Mila Luleva (SoilCares, Wageningen, The Netherlands) is acknowledged for reviewing an earlier version of the manuscript.

**Author Contributions:** Harald van der Werff is the principal author of this manuscript and responsible for the conception and design of this research, as well as data collection, analysis and interpretation. Freek van der Meer contributed to the conception of the idea, as well as discussion of results and review of the manuscript.

**Conflicts of Interest:** The authors declare no conflict of interest.

## References

1. Berger, M.; Moreno, J.; Johannessen, J.A.; Levelt, P.F.; Hanssen, R.F. ESA's sentinel missions in support of Earth system science. *Remote Sens. Environ.* **2012**, *120*, 84–90.
2. Drusch, M.; Del Bello, U.; Carlier, S.; Colin, O.; Fernandez, V.; Gascon, F.; Hoersch, B.; Isola, C.; Laberinti, P.; Martimort, P.; et al. Sentinel-2: ESA's optical high-resolution mission for GMES operational services. *Remote Sens. Environ.* **2012**, *120*, 25–36.
3. Yan, L.; Roy, D.; Zhang, H.; Li, J.; Huang, H. An automated approach for sub-pixel registration of Landsat-8 Operational Land Imager (OLI) and Sentinel-2 Multi Spectral Instrument (MSI) imagery. *Remote Sens.* **2016**, *8*, 520.
4. European Space Agency. ESA Sentinel-2 Delivers First Images. Available online: http://www.esa.int/Our_Activities/Observing_the_Earth/Copernicus/Sentinel-2/Sentinel-2_delivers_first_images (accessed on 28 September 2016).

5. Malenovský, Z.; Rott, H.; Cihlar, J.; Schaepman, M.; García-Santos, G.; Fernandes, R.; Berger, M. Sentinels for science: Potential of Sentinel-1, -2 and -3 missions for scientific observations of ocean, cryosphere, and land. *Remote Sens. Environ.* **2012**, *120*, 91–101.
6. Atzberger, C.; Richter, K. Spatially constrained inversion of radiative transfer models for improved LAI mapping from future Sentinel-2 imagery. *Remote Sens. Environ.* **2012**, *120*, 208–218.
7. Richter, K.; Hank, T.B.; Vuolo, F.; Mauser, W.; D'Urso, G. Optimal exploitation of the Sentinel-2 spectral capabilities for crop leaf area index mapping. *Remote Sens.* **2012**, *4*, 561–582.
8. Richter, K.; Atzberger, C.; Vuolo, F.; Weihs, P.; D'Urso, G. Experimental assessment of the Sentinel-2 band setting for RTM-based LAI retrieval of sugar beet and maize. *Can. J. Remote Sens.* **2009**, *35*, 230–247.
9. Clevers, J.G.P.W.; Gitelson, A.A. Remote estimation of crop and grass chlorophyll and nitrogen content using red-edge bands on Sentinel-2 and -3. *Int. J. Appl. Earth Obs. Geoinform.* **2013**, *23*, 344–351.
10. Frampton, W.J.; Dash, J.; Watmough, G.; Milton, E.J. Evaluating the capabilities of Sentinel-2 for quantitative estimation of biophysical variables in vegetation. *ISPRS J. Photogramm. Remote Sens.* **2013**, *82*, 83–92.
11. Verrelst, J.; Munoz, J.; Alonso, L.; Delegido, J.; Rivera, J.P.; Camps-Valls, G.; Moreno, J. Machine learning regression algorithms for biophysical parameter retrieval: Opportunities for Sentinel-2 and -3. *Remote Sens. Environ.* **2012**, *118*, 127–139.
12. Delegido, J.; Verrelst, J.; Meza, C.M.; Rivera, J.P.; Alonso, L.; Moreno, J. A red-edge spectral index for remote sensing estimation of green LAI over agroecosystems. *Eur. J. Agron.* **2013**, *46*, 42–52.
13. Hill, M. Vegetation index suites as indicators of vegetation state in grassland and savanna: An Analysis with simulated SENTINEL 2 data for a North American transect. *Remote Sens. Environ.* **2013**, *137*, 94–111.
14. Salama, M.S.; Radwan, M.; van der Velde, R. A hydro-optical model for deriving water quality variables from satellite images (HydroSat): A case study of the Nile River demonstrating the future Sentinel-2 capabilities. *Phys. Chem. Earth* **2012**, *50–52*, 224–232.
15. Hedley, J.; Roelfsema, C.; Koetz, B.; Phinn, S. Capability of the Sentinel 2 mission for tropical coral reef mapping and coral bleaching detection. *Remote Sens. Environ.* **2012**, *120*, 145–155.
16. Van der Meer, F.D.; van der Werff, H.M.A.; van Ruitenbeek, F.J.A. Potential of ESA's Sentinel-2 for geological applications. *Remote Sens. Environ.* **2014**, *148*, 124–133.
17. Goetz, A.F.H.; Rowan, L.C. Geologic remote-sensing. *Science* **1981**, *211*, 781–791.
18. Abrams, M. The Advanced Spaceborne Thermal Emission and Reflection Radiometer (ASTER): Data products for the high spatial resolution imager on NASA's Terra platform. *Int. J. Remote Sens.* **2000**, *21*, 847–859.
19. Abrams, M.; Hook, S.J. Simulated ASTER data for geologic studies. *IEEE Trans. Geosci. Remote Sens.* **1995**, *33*, 692–699.
20. Yamaguchi, Y.; Kahle, A.B.; Tsu, H.; Kawakami, T.; Pniel, M. Overview of Advanced Spaceborne Thermal Emission and Reflection Radiometer (ASTER). *IEEE Trans. Geosci. Remote Sens.* **1998**, *36*, 1062–1071.
21. Cudahy, T.; Hewson, R. ASTER geological case histories: Porphyry-skarn-epithermal, iron oxide Cu-Au and Broken Hill Pb-Zn-Ag. In Proceedings of the Annual General Meeting of the Geological Remote Sensing Group (ASTER Unveiled), London, UK, 5–7 December 2002.
22. Mielke, C.; Boesche, N.; Rogass, C.; Kaufmann, H.; Gauert, C.; de Wit, M. Spaceborne mine waste mineralogy monitoring in South Africa, applications for modern push-broom missions: Hyperion/OLI and EnMAP/Sentinel-2. *Remote Sens.* **2014**, *6*, 6790–6816.
23. Van der Werff, H.; van der Meer, F. Sentinel-2 for mapping iron absorption feature parameters. *Remote Sens.* **2015**, *7*, 12635–12653.
24. Immitzer, M.; Vuolo, F.; Atzberger, C. First experience with Sentinel-2 data for crop and tree species classifications in central Europe. *Remote Sens.* **2016**, *8*, 166, doi:10.3390/rs8030166.
25. Clasen, A.; Somers, B.; Pipkins, K.; Tits, L.; Segl, K.; Brell, M.; Kleinschmit, B.; Spengler, D.; Lausch, A.; Förster, M. Spectral unmixing of forest crown components at close range, airborne and simulated Sentinel-2 and EnMAP spectral imaging scale. *Remote Sens.* **2015**, *7*, 15361–15387.
26. Dotzler, S.; Hill, J.; Buddenbaum, H.; Stoffels, J. The potential of EnMAP and Sentinel-2 data for detecting drought stress phenomena in deciduous forest communities. *Remote Sens.* **2015**, *7*, 14227–14258.
27. Dong, T.; Meng, J.; Shang, J.; Liu, J.; Wu, B. Evaluation of chlorophyll-related vegetation indices using simulated Sentinel-2 data for estimation of crop fraction of absorbed photosynthetically active radiation. *IEEE J. Sel. Top. Appl. Earth Obs. Remote Sens.* **2015**, *8*, 4049–4059.

28. Sibanda, M.; Mutanga, O.; Rouget, M. Examining the potential of Sentinel-2 MSI spectral resolution in quantifying above ground biomass across different fertilizer treatments. *ISPRS J. Photogramm. Remote Sens.* **2015**, *110*, 55–65.
29. Du, Y.; Zhang, Y.; Ling, F.; Wang, Q.; Li, W.; Li, X. Water bodies' mapping from Sentinel-2 imagery with Modified Normalized Difference Water Index at 10-m spatial resolution produced by sharpening the SWIR band. *Remote Sens.* **2016**, *8*, 354, doi:10.3390/rs8040354.
30. Toming, K.; Tiit Kutser, T.; Laas, A.; Sepp, M.; Paavel, B.; Nõges, T. First experiences in mapping lake water quality parameters with Sentinel-2 MSI imagery. *Remote Sens.* **2016**, *8*, 640, doi:10.3390/rs8080640.
31. Stratoulias, D.; Balzter, H.; Sykioti, O.; Zlinszky, A.; Tóth, V. Evaluating sentinel-2 for lakeshore habitat mapping based on airborne hyperspectral data. *Sensors* **2015**, *15*, 22956–22969.
32. Rytuba, J.J.; Arribas, A.; Cunningham, C.G.; McKee, E.H.; Podwysocki, M.H.; Smith, J.G.; Kelly, W.C. Mineralized and unmineralized calderas in Spain; Part II, Evolution of the Rodalquilar caldera complex and associated gold-alunite deposits. *Miner. Depos.* **1990**, *25*, S29–S35.
33. Kalinowski, A.; Oliver, S. *ASTER Mineral Index Processing Manual*; Technical Report; Geoscience Australia: Canberra, Australia, 2004.
34. Sabins, F.F. Remote sensing for mineral exploration. *Ore Geol. Rev.* **1999**, *14*, 157–183.
35. Arribas, A.; Cunningham, C.; Rytuba, J.; Rye, R.; Kelly, W.; Podwysocki, M.; McKee, E.; Tosdal, R. Geology, geochronology, fluid inclusions, and isotope geochemistry of the Rodalquilar gold alunite deposit, Spain. *Econo. Geol. Bull. Soc. Econ. Geol.* **1995**, *90*, 795–822.
36. Bedini, E.; van der Meer, F.; van Ruitenbeek, F. Use of HyMap imaging spectrometer data to map mineralogy in the Rodalquilar caldera, southeast Spain. *Int. J. Remote Sens.* **2009**, *30*, 327–348.
37. Debba, P.; Carranza, E.J.M.; Stein, A.; van der Meer, F.D. Deriving optimal exploration target zones on mineral prospectivity maps. *Math. Geosci.* **2009**, *41*, 421–446.
38. Van der Werff, H.; van Ruitenbeek, F.; van der Meijde, M.; van der Meer, F.; de Jong, S.; Kalubandara, S. Rotation-variant template matching for supervised hyperspectral boundary detection. *IEEE Geosci. Remote Sens. Lett.* **2007**, *4*, 70–74.
39. Van der Meer, F. Indicator kriging applied to absorption band analysis in hyperspectral imagery: A case study from the Rodalquilar epithermal gold mining area, SE Spain. *Int. J. Appl. Earth Obs. Geoinform.* **2006**, *8*, 61–72.
40. European Space Agency. Level-2A Prototype Processor for Atmosphericterrain and Cirrus Correction of Top-of-Atmosphere Level 1C Input Data. Available online: http://step.esa.int/main/third-party-plugins-2/sen2cor/ (accessed on 28 September 2016).
41. Schaepman-Strub, G.; Schaepman, M.; Painter, T.; Dangel, S.; Martonchik, J. Reflectance quantities in optical remote sensing—Definitions and case studies. *Remote Sens. Environ.* **2006**, *103*, 27–42.
42. European Space Agency. GMES Sentinel-2 Mission Requirements Document. Available online: http://esamultimedia.esa.int/docs/GMES/Sentinel-2_MRD.pdf (accessed on 28 September 2016).
43. European Space Agency. Sentinel Application Platform (SNAP). Available online: http://step.esa.int/main/toolboxes/snap/ (accessed on 28 September 2016).
44. Harris Geospatial. IDL ENVI Software. Available online: http://www.harrisgeospatial.com/ (accessed on 28 September 2016).
45. Schlapfer, D.; Richter, R. Geo-atmospheric processing of airborne imaging spectrometry data. Part 1: Parametric orthorectification. *Int. J. Remote Sens.* **2002**, *23*, 2609–2630.
46. Richter, R.; Schlapfer, D. Geo-atmospheric processing of airborne imaging spectrometry data. Part 2: Atmospheric/topographic correction. *Int. J. Remote Sens.* **2002**, *23*, 2631–2649.
47. D'Odorico, P.; Gonsamo, A.; Damm, A.; Schaepman, M.E. Experimental evaluation of Sentinel-2 spectral response functions for NDVI time-series continuity. *IEEE Trans. Geosci. Remote Sens.* **2013**, *51*, 1336–1348.
48. Kruse, F.A.; Perry, S.L. Mineral mapping using simulated Worldview-3 short-wave-infrared imagery. *Remote Sens.* **2013**, *5*, 2688–2703.
49. Weather Underground. Weather for Almeria. Available online: http://www.wunderground.com (accessed on 28 September 2016).
50. Arribas, A. *Mapa Geologico del Distrito Minero de Rodalquilar, Almeria, Scale 1:25000*; Instituto Tecnologico GeoMinero de Espana: Madrid, Spain, 1993.

51. Telespazio VEGA Deutschland GmbH. Sentinel-2 MSI—Level-2A Prototype Processor Installation and User Manual. Available online: http://step.esa.int/thirdparties/sen2cor/2.2.1/S2PAD-VEGA-SUM-0001-2.2.pdf (accessed on 28 September 2016).
52. DigitalGlobe. Worldview–3. Available online: http://worldview3.digitalglobe.com/ (accessed on 28 September 2016).
53. AuScope Limited. AuScope Discovery Portal. Available online: http://portal.auscope.org/portal/gmap.html (accessed on 28 September 2016).